J Mater Sci (2018) 53:2181–2192

Metals

Helical gold nanotube film as stretchable micro/nanoscale strain sensor

Chenghao Deng[1], Lujun Pan[1,*], Chengwei Li[1], Xin Fu[1], Ruixue Cui[1], and Habib Nasir[2]

[1] School of Physics, Dalian University of Technology, No. 2 Linggong Road, Ganjingzi District, Dalian 116024, People's Republic of China

[2] School of Natural Sciences, National University of Sciences and Technology, H-12 Sector, Islamabad, Pakistan

Received: 23 August 2017
Accepted: 5 October 2017
Published online: 12 October 2017

ABSTRACT

A micro/nanoscale strain sensor based on helical gold nanotube films (GNTFs) is proposed, which is prepared by magnetron sputtering using carbon nanocoils (CNCs) as templates. The gauge factor of the sensor reaches 5, while the stretch of it can achieve more than 10% owing to the helical geometries. The resistance increase of GNTFs with temperature decreasing from 300 to 4 K indicates a thermal activation tunneling model for electron transport. With thicknesses increasing from 16 to 32 nm, the GNTFs show a structural transition from discontinuous to quasi-continuous film. In this transition region, the conductive path of GNTFs increases rapidly, resulting in a rapid resistance decrease of CNC–GNTF composite structure. When a helical GNTF is stretched, the resistance is increased. The helical GNTFs in the transition region exhibit the highest response sensitivity, which owes to the special torsion-dominated strains of this helical structure to some extent. The unique helical morphology gives the sensor great stretchability and special electrical response. Choosing appropriate CNCs and GNTFs with suitable thickness, the helical GNTFs can be used as micro/nanostretchable strain sensors, stretchable electrodes or connects, resonators in micro/nanoelectromechanical system.

Introduction

Flexible strain sensor is an advanced sensor technology accompanying with the development of smart sensor system, which has played more and more significant roles in wearable instruments [1], e-skins [2, 3], robots [4], energy-harvesting systems [5, 6] and touch-on displays [7, 8]. Recently, the applications of micro/nanomanufacturing techniques in flexible substrates provide a wide development space for new strain sensors with small size, large deformation, high sensitivity, low power and easy integration.

Gold film has been a research focus for strain sensors with high sensitivity and flexibility [9–12]. The gold film has three types of structure, which are continuous film, quasi-continuous film and nanoisland array, where the electron transport is determined by surface scattering, conductive path

Address correspondence to E-mail: lpan@dlut.edu.cn

DOI 10.1007/s10853-017-1660-y

between gold nanoparticles and tunneling effect between islands, respectively [13]. Due to the differences in structure and thickness, the gauge factors of gold films are varied between 1 and 300. Parker and Krinsky [14] studied the electrical resistance-strain characteristics of thin gold films prepared by vacuum evaporation. Varying the thickness of gold film, the gauge factor changed from 1 to 100. The discontinuous gold film with a thickness less than 10 nm showed the highest gauge factor due to the exponentially dependence of resistance on separation space between gold particles. Neugebauer et al. proposed different conductive mechanisms for the evaporated gold films with different thicknesses, which transformed from electron tunneling to essential bulk conduction with thickness increasing [13].

Due to the original non-continuity, the highest gauge factor and the ability to bear large deformation without permanent damage on structure, the discontinuous films drew much attention in the field of flexible sensors. However, the gold nanoparticles in this type of discontinuous film tend to migrate to form larger islands and consequently to reduce the gauge factor. For solving this problem, monolayer or multilayers of self-assembled gold nanoparticles with dielectric between them on flexible substrates were developed [15–17]. Brust et al. prepared self-assembled multilayer thin films consisting of 6-nm gold nanoparticles and dithiols. This kind of film shows a mode of activated electron hopping [18]. Herrmann et al. [19] prepared film of 18-nm gold nanoparticles using inkjet printing and demonstrated its exponential sensitivity of the electrical resistance to longitudinal deformation, determining the gauge factor to be varied between 50 and 200. Jiao et al. [20] reported the strain gauge made up of 50 nm gold nanoparticle monolayer on the flexible polyethylene terephthalate substrate, which can accurately track various mechanical stimuli and achieved a high gauge factor up to 70.

However, the size and application of these strain gauges based on gold films are mainly in macroscale. In micro/nanoscale, the electrical responses to local tension for some nanomaterials were reported [21–23]. However, their applications were limited by their tensile abilities. The gold film-based flexible strain sensor using super nanospring [carbon nanocoil (CNC)] as carrier or template provides an idea for solving this problem. CNC is a kind of carbon nanotubule with a unique 3D helical structure, which shows excellent mechanical [24–26], electrical [27, 28] and thermal properties [29]. As a super nanospring, the large elastic expansion up to 40% and superior fatigue resistance of a CNC make it a great candidate for the application in nanoscale flexible sensor and MEMS/NEMS. When a CNC is longitudinally stretched, the strains of the CNC consist of tension, shear, bending and torsion, due to the helical morphology [25]. The gold film on a helical nanowire would exhibit quite different electrical response under tension compared to those on macroplanar substrates. In addition, the ability that transforms the unidirectional deformation into torsion which cannot be achieved by other micro/nanostructures brings CNC great advantage in strain sensor research. In this research, we developed helical gold nanotube films (GNTFs) using CNCs as templates. The resistance response to strains and the electron transport of the helical GNTFs are investigated.

Experimental

CNC synthesis by chemical vapor deposition (CVD) method

The CNCs were synthesized by a CVD method [30]. 0.2 mol/L solution consisting of $Fe_2(SO_4)_3{\cdot}9H_2O$, $SnCl_2{\cdot}5H_2O$ and deionized water was served as the catalyst precursor. The catalyst was first dipped on the quartz substrate and then calcined at 710 °C for 30 min in an argon atmosphere with an Ar flow rate of 365 sccm. At last, the carbon deposits were achieved at 710 °C for 1 h by introducing acetylene and Ar gases with flow rates of 15 and 325 sccm, respectively.

Helical GNTF preparation

The GNTFs were deposited onto individual CNCs by magnetron sputtering. Three parameters, which are sputtering time, pressure in sputtering chamber and temperature of substrate, were modulated in sequence to control the thickness and gold particle size of GNTFs, while the sputtering power was fixed at 20 W. The sputtering time was increased from 0.5 to 16 min. The film thickness and gold particle size were all changed with the sputtering time. As proposed in some works, the sensitivity of nanoparticles

based strain gauges is proportional to the diameter of nanoparticles. It is reasonable to evaluate that the helical GNTF with larger particle size will exhibit larger sensitivity as well in this research. To achieve the largest gold particle size, the pressure and temperature were varied from 1 to 4 Pa and from RT to 300 °C, respectively, with 4 min sputtering time. The relationship between GNTF thickness and sputtering time was determined by measuring the thickness of GNTF deposited on silicon dioxide substrate with an atomic force microscope (AFM). To observe the morphology of GNTFs on CNCs, scanning electron microscope (SEM) and transmission electron microscope (TEM) were employed. For sample preparation, CNCs were dispersed onto copper micro grid, followed by gold sputtering onto their surfaces. The size of gold particles was counted.

Resistance of helical GNTF and its response to tension

As shown in Fig. 1a, an individual CNC was first extracted from an as grown CNC bush by a micro-tungsten probe with silver paste under an optical microscope. Then, a gold film was pre-sputtered on the individual CNC by 2 min at 2 Pa and RT. After that, the individual CNC with GNTF was suspended between two electrodes by silver paste with the help of micromanipulators. The composite structure of CNC and GNTF is called C-GNTF in this paper. The electrodes which were made of glass slices with 100-nm gold film on the surfaces were fixed on a larger glass substrate with a hole in the middle. This hole was designed for repeated sputtering. The distance between the two electrodes was 50 to 100 μm. Figure 1c shows the SEM image of a typical sample.

The resistance of the C-GNTF sample with 2 min gold pre-sputtering was measured with a source meter (Agilent B2902A). After the resistance measurement, the sample was sputtered again for another 2 min while the sputtering condition kept the same as before. The resistance of the sample was measured after every 2 min sputtering till the total sputtering time reached 14 min.

As shown in Fig. 1a, b, an insulated microprobe was employed to stretch the C-GNTF transversely in the middle under the optical microscope with the help of a micromanipulator. The current fed through the sample was 1–3 μA. The deformation of the C-GNTF was monitored by a CCD camera, while the resistance of the sample was recorded by the source meter simultaneously. The resistance response under lateral tension of the same sample after different time sputtering was measured. However, the resistance of CNC itself will greatly reduce the sensitivity of resistance response due to the parallel connection between CNC and GNTF. Thus, a 15-nm layer of Al_2O_3 acting as an insulation layer was sandwiched between CNC and GNTF to eliminate the influence of CNC. The Al_2O_3 layer was sputtered onto a CNC by magnetron sputtering at 1 Pa and RT with a sputtering power of 100 W. For distinguishing, the composite structure with an Al_2O_3 layer is called A-GNTF. The resistance response under lateral tension of A-GNTFs was also measured.

The measurements mentioned above were based on a two electrode method, the results of which could be affected by the contact resistance between GNTF and gold electrodes. It is difficult to apply four electrodes to a lateral tension measurement. Based on the optimal thickness and structure of GNTF determined by the resistance response under lateral tension, a four-electrode method was employed in a longitudinal tension measurement to verify the sensitivity. As schematically shown in Fig. 1d, an A-GNTF with optimal thickness and structure was connected between two tungsten probes with silver paste. Two flexible carbon nanotube (CNT) bundles attached on the tips of tungsten probes were employed as sensing probes [31], which were attached to the A-GNTF by van der Waals forces. The A-GNTF was longitudinally stretched by the tungsten probes, while the CNT bundles moved with the stretching of A-GNTF.

Electron transport of helical GNTF

To investigate the electron transport of helical GNTF, the resistance of individual A-GNTFs was measured from 300 to 4 K in a closed cycle refrigerator system. The resistance of the A-GNTF at different temperature was recorded by the source meter under a constant current of 2 μA.

Strain analysis of CNC

To further characterize the resistance response of a helical GNTF to extension, strain analysis was carried out. Due to the helical morphology of CNC, the total tension is a combination of four types of strains. Chen et al. [25] have studied the axial stretch of CNC under

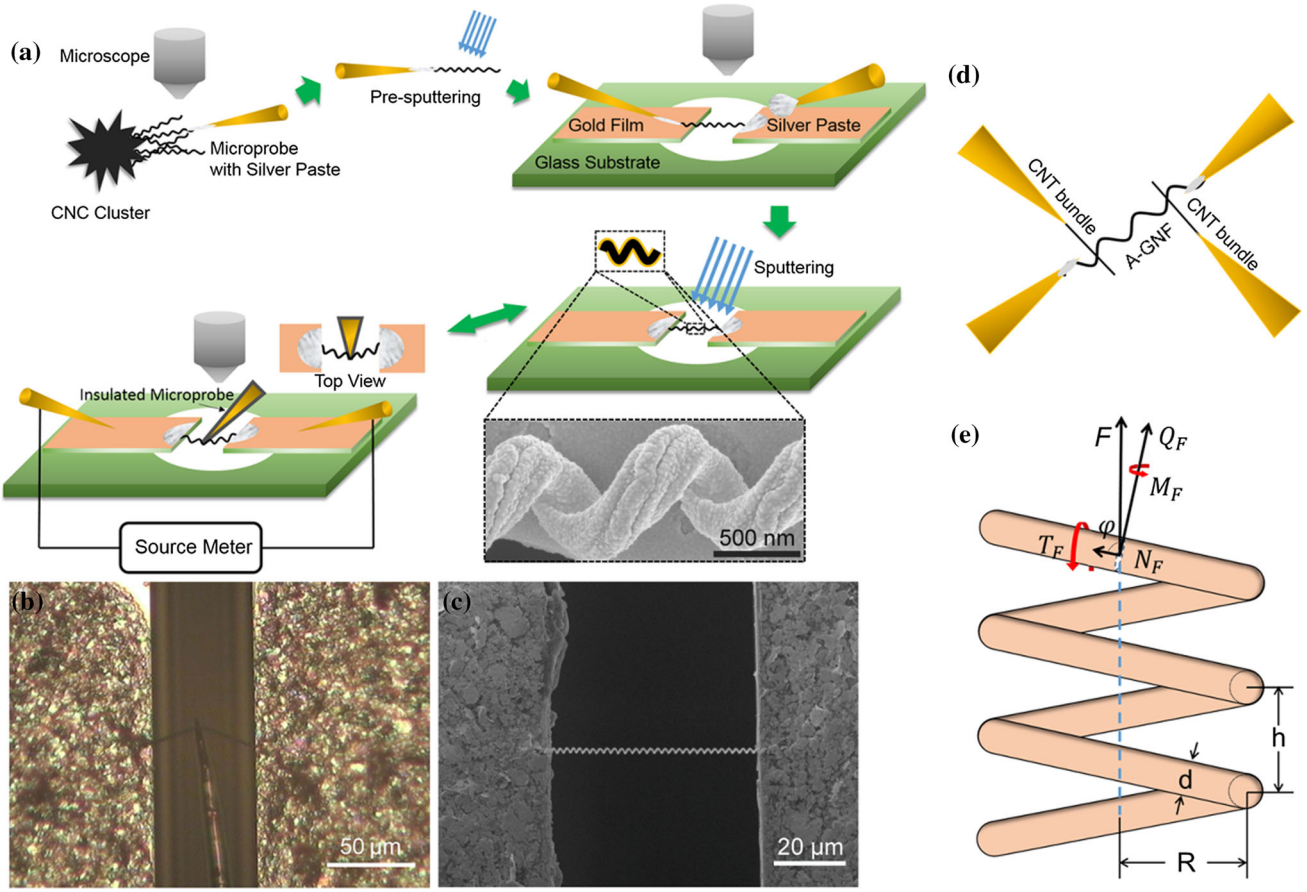

Figure 1 **a** Schematic of sample preparation and resistance response measurement under lateral tension. **b** CCD image of resistance response measurement for a CNC under an optical microscope. **c** SEM image of a typical sample. **d** Schematic of resistance response measurement of A-GNTF by the four-electrode method under longitudinal tension using flexible CNT bundle as sensing probe. **e** Schematic representation of the CNC as a helical spring and the resultant forces at the cross section.

an axial tensile load with material mechanics. As shown in Fig. 1e, there are four types of acting forces on the cross section of the coil,

$$N_F = F \cdot \cos\phi = \frac{FH}{\sqrt{R^2+H^2}}$$

$$Q_F = F \cdot \sin\phi = \frac{FR}{\sqrt{R^2+H^2}}$$

$$M_F = F \cdot \cos\phi \cdot R = \frac{FRH}{\sqrt{R^2+H^2}}$$

$$T_F = F \cdot \sin\phi \cdot R = \frac{FR^2}{\sqrt{R^2+H^2}}$$

where N_F, Q_F, M_F and T_F are the tension force, shear force, bending moment and torsion moment, respectively. F, R and φ are the tensile load, coil radius and helical angle of the coil, respectively. $H = h/2\pi$, where h is the pitch of the coil. Normal strain induced by tension force and shear strain induced by shear force are expressed as,

$$\varepsilon_N = \frac{N_F}{EA} = \frac{FH}{EA} \times \frac{1}{\sqrt{R^2+H^2}} \quad (1)$$

$$\varepsilon_Q = \frac{\alpha_s Q_F}{GA} = \frac{\alpha_s FR}{GA} \times \frac{1}{\sqrt{R^2+H^2}} \quad (2)$$

where E, G, α_s and A are the Young's modulus, shear modulus, shear coefficient and cross-sectional area of the coil. $A = \pi d^2/4$, where d is the line diameter of the coil. $\alpha_s = (7+6\upsilon)/6(1+\upsilon)$, where υ is the Poisson ratio. $E = 2(1+\upsilon)G$. The strains induced by tension and shear force keep equal in the cross section.

The bending and torsion moments induce normal and shear strains, respectively, which vary in the cross section from point to point. The value of bending and torsion induced strains is related to the position of the measured point, which needs complex analysis. For simplicity, the maximum normal and shear strains in the cross section are calculated as,

$$\varepsilon_M = \frac{M_F}{EI} \times \frac{d}{2} = \frac{FRHd}{2EI} \times \frac{1}{\sqrt{R^2 + H^2}} \quad (3)$$

$$\varepsilon_T = \frac{T_F}{GJ} \times \frac{d}{2} = \frac{FR^2d}{2GJ} \times \frac{1}{\sqrt{R^2 + H^2}} \quad (4)$$

where I and J are the moment and polar moment of inertia of the cross section, respectively, when $I = \pi d^4/64$ and $J = \pi d^4/32$. The maximum values of ε_M and ε_T are distributed on the surface of CNC.

The tensile load applied on the CNC is expressed as,

$$F = K_0 h \frac{\Delta L}{L}$$

where K_0 is the spring constant of each coil in the CNC. $\Delta L/L$ is the length expansion of the CNC. Giving the length expansion and geometric parameters, the normal and shear strains of the CNC can be calculated.

It is noted that the strains on CNC vary from point to point. For more intuitionistic and comprehensive point of view, a finite element analysis (FEA) based on Comsol 3.5 was carried out to simulate the strain response of CNC. The model of CNC was established in Matlab. Then, the model was imported into Comsol 3.5. The CNC was longitudinally stretched by 5%.

Results and discussion

Morphology of GNFs and size of gold particles under different sputtering conditions

Figure 2a shows the SEM images of GNTFs coated on CNCs under different sputtering time at 1 Pa and RT. The growth of gold on the surface of CNC corresponds to Volmer–Weber island growth mode, which can be clearly seen from the SEM images. With sputtering time increasing, the nanoparticles keep growing, with interspace decreasing. The nanoparticles are basically separated before 4 min sputtering. The film sputtered by 4 min shows the most obvious grainy morphology. When the sputtering time exceeds 4 min, the interspace between gold particles is gradually filled with new gold nanoparticles. The gold film becomes to be continuous and smooth. Figure 2b is the TEM images of the GNTF on CNC at 2-min sputtering time, where a thin layer of GNTF on the surface of CNC can be observed. Good lattice inside a nanoparticle can be seen from the lower image. The inter-planar spacing is estimated to be 0.236 nm, corresponding to that of the (111) planes of gold (0.235 nm).

Figure 2c presents the relationship between the thickness of GNTFs and the sputtering time, which determines the sputtering speed to be 4 nm/min. The diameter of gold nanoparticles was counted for different sputtering time, as shown in Fig. 2d. The gold nanoparticles keep growing till the sputtering time reaches 4 min, when the particle size reaches 16.71 nm which is almost equal to the film thickness at 4 min. Then, the particle size tends to be stable after 4 min sputtering. Because the gradually filled interspace obscures the boundary of the particles, it becomes difficult to measure the size of nanoparticles with sputtering time increasing after 4 min. The inset in Fig. 2d shows the histogram of nanoparticles' sizes for the gold film sputtered by 6 min. The particle size ranges from 13 to 20 nm, and the average size is 16.43 nm.

Figure 2e is the size of gold particles at different sputtering pressures, while the sputtering time and the temperature of substrate are fixed at 4 min and RT, respectively. It is found that the particle size reaches the largest at 2 Pa. Then, fixing the sputtering time and pressure at 4 min and 2 Pa, respectively, the temperature was increased from RT to 300 °C. The particle size increases slowly with the rise of temperature, as shown in Fig. 2f. The increase in deposition speed at 2 Pa accounts for the increase in particle size, while the increase in temperature promotes the surface diffusion, resulting in the increase in particle size. Considering the small size increase induced by the temperature rise and the bearing ability of samples in high temperature, the following sputtering was conducted at RT and 2 Pa.

Characterization of resistance and electron transport of GNFs

From the SEM images and the results of size statistics, it is considered that a transition of GNTF from discontinuous to quasi-continuous film occurs when the film thickness increases from 16 to 32 nm. For further demonstration of the transition, the resistance of a C-GNTF sample with different film thickness was measured. The C-GNTF sample exhibits linear I–V characteristic curve (inset of Fig. 3a). The noise

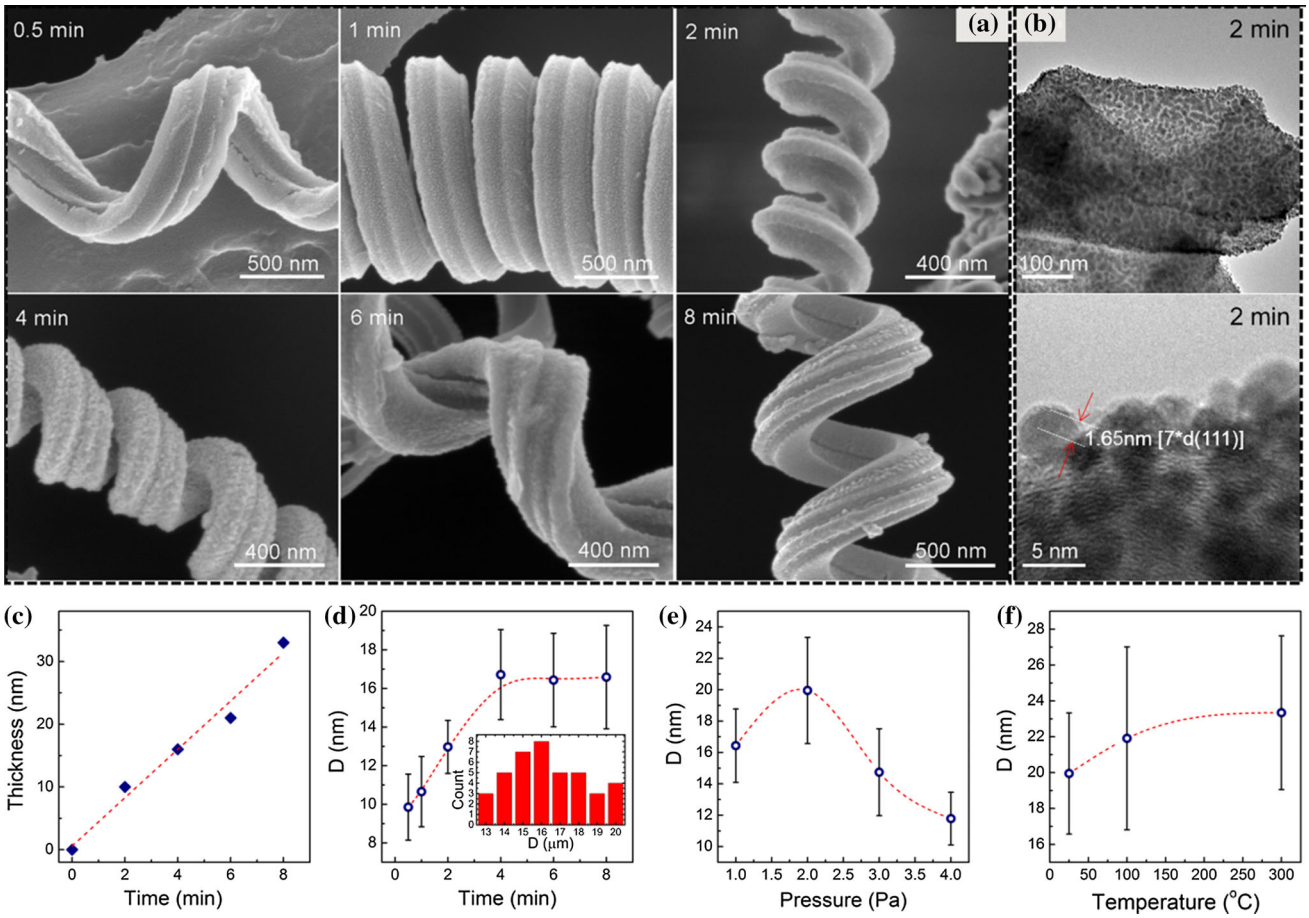

Figure 2 **a** SEM images of GNTF on the surface of CNC at different sputtering times. **b** TEM images of GNTF. **c** Thickness of GNTF at different sputtering times. Gold particle size at different **d** sputtering times, **e** pressure and **f** temperature. The inset in **d** is the histogram of nanoparticles' sizes for the gold film sputtered by 6 min.

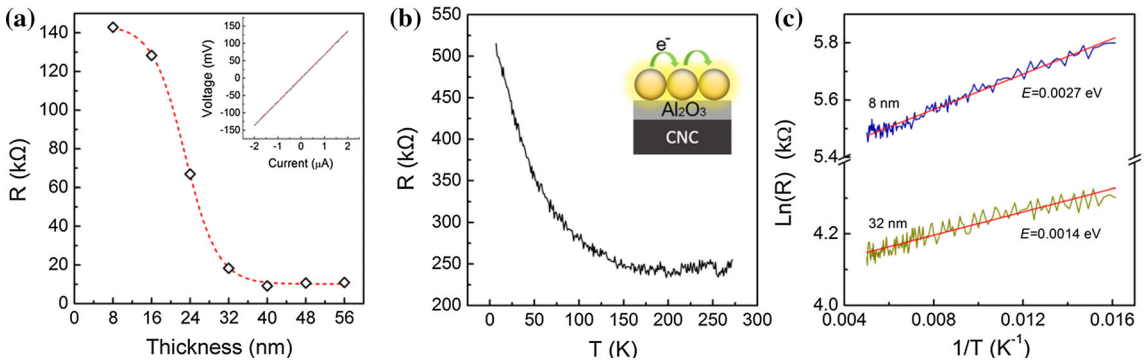

Figure 3 **a** Resistance of a C-GNTF sample at different film thicknesses. The inset is the *I*–*V* characteristic curve of the sample. **b** Temperature-dependent resistance of an A-GNTF sample with a film thickness of 8 nm. **c** Exponential relationship between the resistance and temperature of two A-GNTF samples with film thicknesses of 8 and 32 nm.

during measurements introduces an error of voltage within 2%. As shown in Fig. 3a, when the thickness of the GNTF increases from 8 to 56 nm, the resistance of the sample decreases from 143 to 11 kΩ. The appearance electrical resistivity of the C-GNTF at thickness of 8 nm in Fig. 3a is 9.2×10^{-5} Ω m, which is comparable to that of the CNCs reported in Ref. [24]. Thus, the resistance change induced by gold

particles is very little when the thickness is less than 8 nm, which is considered to be originated from the discontinuous structure of the GNTF. A rapid resistance decrease with thickness increasing from 16 to 32 nm can be seen from Fig. 3a. When the film thickness exceeds 32 nm, the resistance changes slightly with thickness increasing, the reason for which is considered as the almost invariable resistivity after the transition from discontinuous to quasi-continuous film.

For further demonstrating the structural change, the temperature dependence of the resistance for GNTF was measured. Figure 3b is the resistance of an A-GNTF with a film thickness of 8 nm. The resistance increases with temperature decreasing, indicating a thermal activation tunneling of electron transfer. The resistance of GNTF can be expressed as $R = R_0 \exp(E/kT)$, where E is the activation energy and k is the Boltzmann constant. Figure 3c shows the linear relationship between LnR and $1/T$ for two A-GNTF samples with film thicknesses of 8 and 32 nm, determining the activation energies of 0.0027 and 0.0014 eV, respectively. The reduced activation energy indicates a reduced tunneling barrier for electrons from particle to particle, resulted from the increase in particle size and decrease in interspace between particles. The reduced activation energies induce very little resistance change as calculated. Thus, the rapid resistance decrease with thickness increasing from 16 to 32 nm is mainly due to the increase in conductive path density [32].

Resistance response of GNFs under transverse tension

Considering the transition of GNTFs from discontinuous to quasi-continuous film and the rapid resistance decrease of C-GNTFs in this transition region, the resistance responses to strains of C-GNTFs with film thicknesses of 16, 24 and 32 nm were measured to investigate the change in response sensitivity with the increase in gold film thickness. Figure 4a shows the resistance response of a C-GNTF sample with 16 nm thick film for 7 cycles. After repeating for 4 times, the resistance response becomes stable. The initial resistance for cycles 4–7 keeps at 63.8 kΩ. Considering the measurement error, the resistance responses for cycles 4–7 are essentially the same. The length of the C-GNTF was measured from the CCD image by 10 times and taken as the average value, within 2% error. The length expansion of C-GNTFs is less than 10% in the experiments. The resistance changes linearly with the length expansion. The ratio of relative resistance change to length expansion is defined as gauge factor "g." $g = (\Delta R/R_0)/(\Delta L/L_0)$, where R_0 and L_0 are the initial resistance and length of the C-GNTF, respectively. The value of g is obtained from linear fitting of the seventh cycle to be 0.41 for the sample shown in Fig. 4a.

Figure 4b–d shows the results of tension tests for 7 CNC samples with 16, 24 and 32 nm thick gold film. The relative resistance change shows good linear relation with the length expansion. The samples with 32 nm film thickness show the smallest sample to sample variation. The average gauge factors for the C-GNTF samples at film thickness of 16, 23 and 32 nm are 0.46, 0.86 and 0.35, respectively, as shown in Fig. 4g. Figure 4e and f shows the resistance responses of two C-GNTF samples (sample 1 and sample 2) at different film thicknesses. The gauge factors for sample 1 at film thicknesses of 16, 24 and 32 nm are 0.31, 0.99 and 0.34, respectively, while those for sample 2 are 0.32, 0.53 and 0.34, respectively. The gauge factor at film thickness of 24 nm is significantly larger than those at thicknesses of 16 and 32 nm. In the transition region, the conductive path increases rapidly with film thickness. The GNTFs with 24 nm film thickness have more chance to change from quasi-continuous state to discontinuous state under strain, resulting in a separation of gold particles. This determines the significantly higher gauge factor for 24-nm-thickness film. When the film thickness is fixed, the resistance response of C-GNTFs is affected by two parameters, which are the helix geometries and initial resistance of the CNCs. The differences in resistance responses between sample 1 and sample 2 are owed to these two parameters.

As the resistance and its response to tension for C-GNTFs are affected by the initial resistance of CNCs due to the parallel connection between the CNC and GNTF, it is necessary to eliminate the influence of the initial resistance of the CNC. For this purpose, a 15-nm layer of Al_2O_3 as an insulation layer was sandwiched between CNC and GNTF. Figure 5a shows the resistivity of A-GNTFs with different film thicknesses. Due to the essentially insulated nature of the Al_2O_3 layer, it is necessary to sputter a layer of

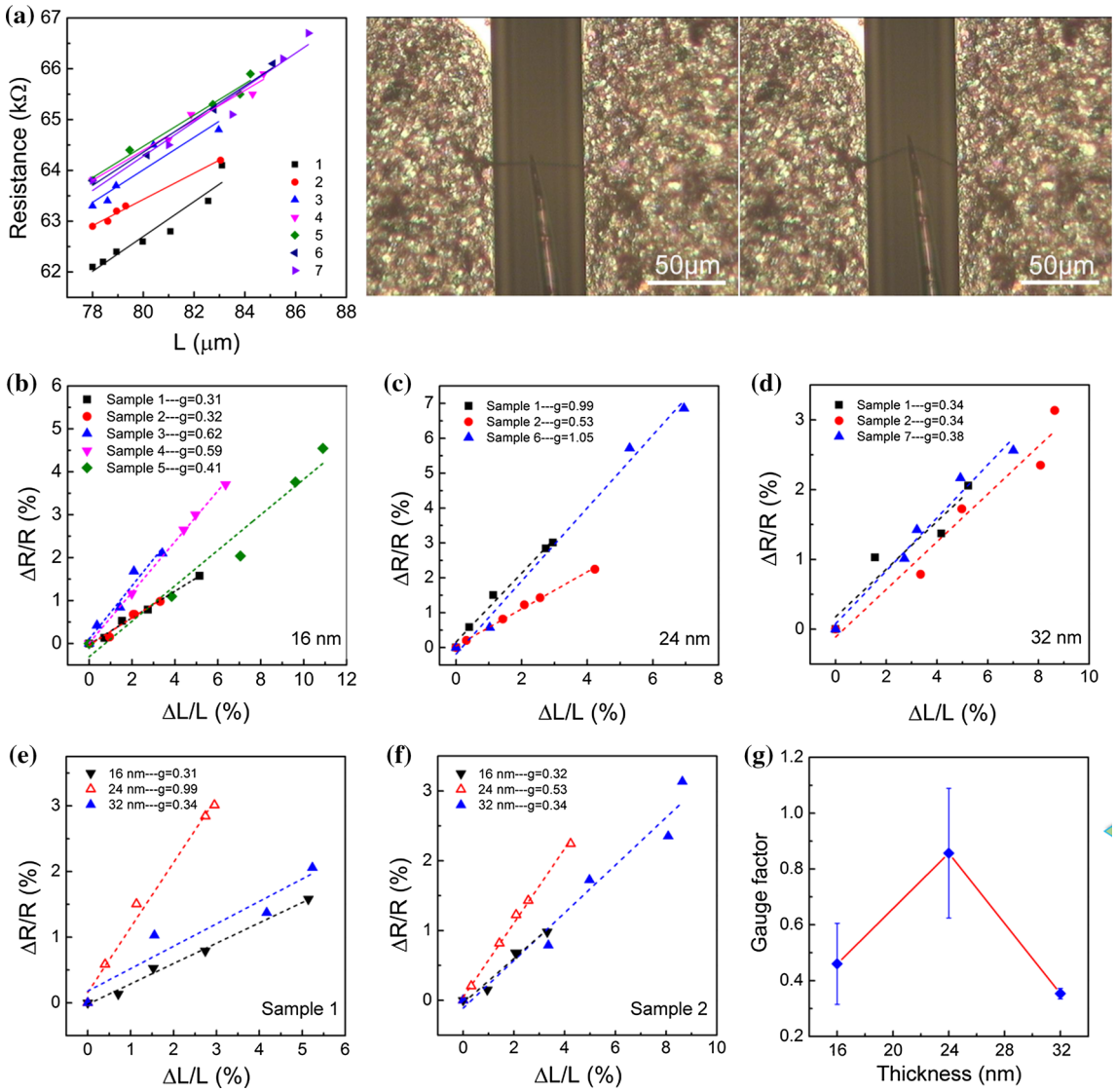

Figure 4 **a** Resistance responses to length expansion of a C-GNTF sample with film thickness of 16 nm. Resistance responses to length expansion of C-GNTF samples with film thickness of **b** 16 nm, **c** 24 nm and **d** 32 nm. Resistance responses of **e** sample 1 and **f** sample 2 at different film thicknesses. **g** Gauge factors at different film thicknesses.

Figure 5 **a** Resistivity of A-GNTFs at different film thicknesses. **b** Resistance responses of two A-GNTF samples with film thicknesses of 24 nm (sample 8) and 16 nm (sample 9).

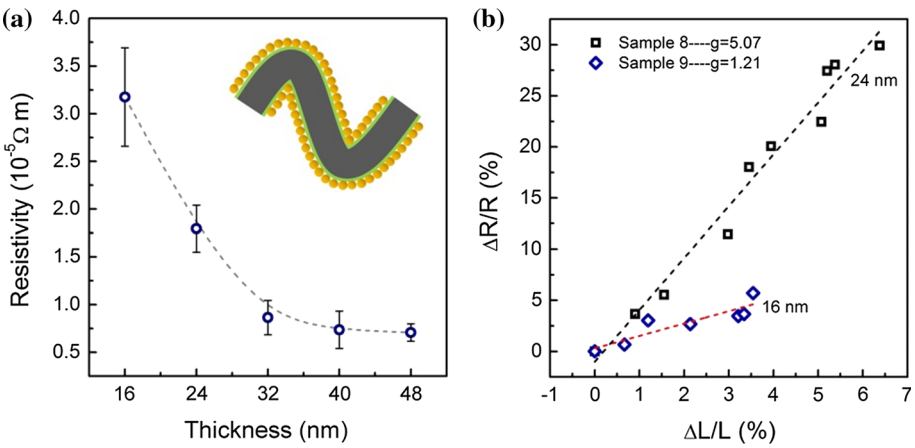

GNTF with enough thickness (at least 16 nm thick in this research) on the surface of the Al_2O_3 layer before fixing the sample onto electrodes to ensure the good electrical contact between the sample and the electrodes. The resistivity of A-GNTFs decreases rapidly from 3.18×10^{-5} to 0.86×10^{-5} Ω m with film thickness increasing from 16 to 32 nm. Figure 5b shows the resistance responses of two A-GNTF samples (samples 8 and 9) with film thicknesses of 24 and 16 nm, respectively. The gauge factors for the two samples are 5.07 and 1.21. After eliminating the influence of the resistance of CNC, the gauge factor is improved by several times. However, it is noted that the significant decrease in the gauge factor for C-GNTFs cannot be simply explained by a parallel connection. As a composite structure, CNC and GNTF cannot be treated separately. On the other hand, the morphology of GNTF on the Al_2O_3 layer may have differences compared to that on the surface of CNC, which has not been systematically studied in this research.

Verification of resistance response sensitivity by a four-probe method

To eliminate the influence of contact resistance and verify the results obtained before, a four-electrode method was employed in the resistance measurement for A-GNTFs under longitudinal tension. As shown in the inset of Fig. 6a, two flexible CNT bundles are attached to an A-GNTF sample firmly and move with the stretch of the A-GNTF. The sample was first stretched and then recovered to initial length. The stretching process was recorded by a CCD camera. Figure 6a presents the resistance evolution recorded by the source meter of the A-GNTF sample (sample 10) with film thickness of 24 nm. We applied cyclic loading–unloading tests to the sample. With the stretching process, the resistance of the sample is first increased from 91 kΩ to a higher value and then decreased to 91 kΩ. In the 5 cycles, the resistance of the sample at unloading state keeps around 91 kΩ. Figure 6b is the resistance response to length expansion of sample 10. From the linear fitting, the gauge factor of sample 10 is determined to be 5.18.

Strain analysis for GNFs under tension

It is difficult to analyze the strains of CNC under transverse tension when the deformation varies along the length direction. For convenience, the strain analysis for a CNC under longitudinal tension is carried out. When the resistance changes linearly with tension, the total resistance change will be proportional to the total deformation no matter how the deformation varies along the length direction. Thus, it is reasonable to use longitudinal tension analysis to describe transverse tension. Figures 7a–c shows the relationship between the strains on CNC and its geometries, calculated from Eqs. (1) to (4). The CNC is stretched by 5%. The torsion and bending strains mean the maximum shear and normal strains on the CNC induced by torsion and bending moments, respectively. The line radius r, coil radius R and pitch h are varied in the strain calculation. Two of the geometric parameters are fixed when the other one is modulated. The fixed line radius, coil radius and pitch are 150, 400 and 800 nm, respectively. All the strains are less than 1%, as seen from Fig. 7a–c. The torsion strain dominates while the tension strain is much less than the other three strains. The shear strain and bending strain have the similar value. All

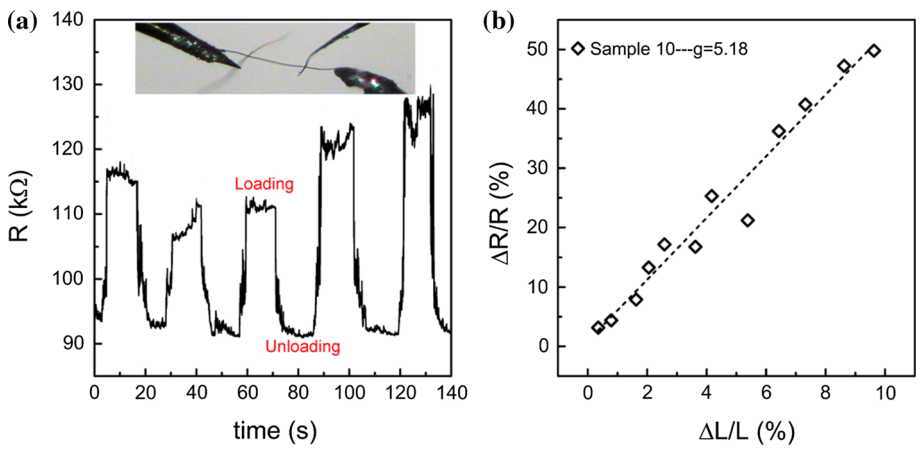

Figure 6 **a** Resistance evolution and **b** its relationship with length expansion of an A-GNTF sample (sample 10) under longitudinal tension tests. The inset in **a** is the CCD image of the longitudinal tension tests using CNT bundles as sensing probes.

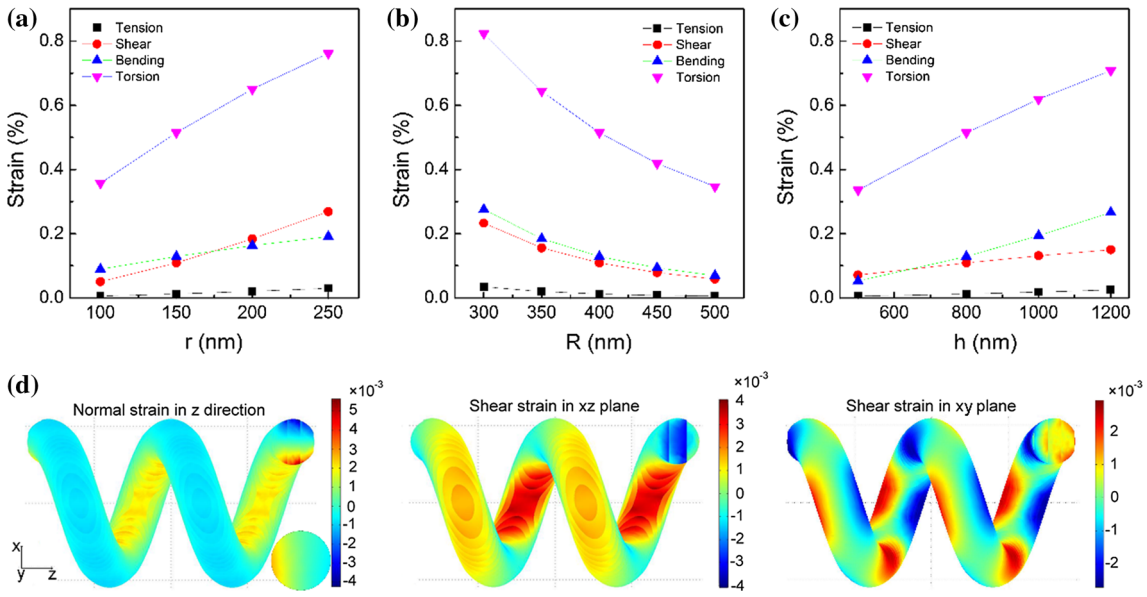

Figure 7 Relationship between strains and **a** line radius, **b** coil radius and **c** pitch. **d** FEA results of strains for a CNC ($r = 150$ nm, $R = 400$ nm, $h = 800$ nm).

the strains show positive relation with line radius and pitch, and negative relation with coil radius. In other words, the more the CNC like a spring, the less strains will be. For practical CNCs used in the experiments, the torsion strain is around 2%, and the other strains are always less than 1%. For a practical CNC used in the research ($r = 220$ nm, $R = 327$ nm, $h = 1.8$ μm), the contribution to total strains made by torsion, shear, bending and tension are 45, 18, 32 and 5%, respectively.

Figure 7d shows the FEA results of strains for a CNC with 150 nm line radius, 400 nm coil radius and 800 nm pitch. The CNC is stretched by 5%. The values of strains are close to those calculated from the theoretical analysis. From the normal strain in Z direction, it is seen that the inside of the coil is stretched, while the outside is compressed. From the center to the surface of the fiber, the strain increases gradually. The absolute value of the normal strain in the inner side is larger than that in the outer side. That means the GNTF is stretched overall. From the local point of view, the resistance of the GNTF in the outer side may be decreased when the GNTF is compressed. However, the total resistance of the helical GNTF is increased when the GNTF is stretched overall, as revealed by the experiments. The two figures on the right of Fig. 7d are the shear strains on CNC. We only discuss the absolute value of shear strain here when the sign of the value is related the direction. From the inner side to outer side, the shear strain decreases from 0.40% (inner side) to 0.25% (the left and right sides of the cross section) then to 0.15% (the outer side). It is easy to understand the change in shear strain. Considering the helical morphology, the length of the fiber is gradually increased from the inner side to the outer side of the coil. Assuming the deformation keeps equal in the cross section, the fiber in the inner side with smaller length will experience larger strain. The difference in the normal and shear strains between different parts of the fiber will be smaller with the line radius decreasing.

The strain gauges made of deposited metal film or metal nanoparticle film have been widely researched, which are based on the tension strain of the film on the surface of a flexible substrate. The electron tunneling for discontinuous film and the electron scattering for continuous thin film between metal particles are sensitive to tension. It has been proposed that the sensitivity of deposited metal film-based strain gauges decreases first and then increases with thickness increasing. The lowest sensitivity lies in the transition region from discontinuous to continuous film. However, the helical GNTF is a completely different strain system, which holds four types of strains simultaneously. The torsion and shear strains dominate the total strains. On the other hand, the surface of CNCs is a high curvature surface for gold nanoparticles when the perimeter of CNCs is only

about 60 times of the particle size. The GNTF on CNC may exhibit quite different electrical response compared to that on macroplanar substrate under the same strain. It seems that the torsion-dominated strains could more easily change the electron tunneling between gold particles and the network of conductive path for the GNTFs in the transition region. For completely discontinuous helical GNTF, the resistance response has not been measured due to the significant influence of CNC's resistance for C-GNTFs and the effect of contact resistance and instability for A-GNTFs.

The helical GNTFs sensitive to strains can be used as flexible micro/nanostrain sensing elements, while those insensitive to strains show potential applications as flexible electrodes or connects. With the thickness increasing, the resistance of GNTFs keeps decreasing to a very small level when the C-GNTFs can be used as microelectrodes or connects. The resistance change under tension of C-GNTFs will be negligible when the GNTF and the CNC are thick and spring-like enough, respectively. On the other hand, the spring-like characteristics of helical GNTF bring it great flexibility no matter how it will be used.

Conclusions

Helical GNTFs were prepared by depositing gold film onto CNCs using magnetron sputtering. A transition from discontinuous film to quasi-continuous film of GNTF was observed when the thickness increased from 16 to 32 nm. In this transition region, a rapid resistance decrease of C-GNTF was found due to the significant increase in conductive path. The resistivity of GNTF decreased rapidly from 3.18×10^{-5} to $0.86 \times 10^{-5}\ \Omega\,m$ with thickness increasing from 16 to 32 nm, accompanied with the decrease in electron tunneling barrier between gold particles. The GNTFs with a film thickness of 24 nm showed the highest gauge factors which reached 5, corresponding to the point that the conductive path increases fast with thickness increasing. The torsion strain dominates the total strains, which is generally around 2% for practical CNCs stretched by 5%. The shear, bending and tension strains are always less than 1%. The unique strains owing to the helical morphology and the high curvature surface of helical GNTFs result in the different electrical responses of the helical GNTFs compared to those on macroplanar substrates. Choosing appropriate CNCs and GNTFs with suitable thickness, the helical GNTFs can be used as micro/nanostretchable strain sensing elements or stretchable electrodes or connects.

Acknowledgements

This work was supported by the National Natural Science Foundation of China (Nos. 51661145025, 11274055, 61520106013).

Compliance with ethical standards

Conflict of interest The authors declare that they have no conflict of interest.

References

[1] Gong S, Schwalb W, Wang Y, Chen Y, Tang Y, Si J (2014) A wearable and highly sensitive pressure sensor with ultrathin gold nanowires. Nat Commun 5:4132–4139

[2] Walker G (2012) A review of technologies for sensing contact location on the surface of a display. J Soc Inf Disp 20:413–440

[3] Kim D, Lu N, Ma R, Kim Y, Kim R, Wang S (2011) Epidermal electronics. Science 333:838–843

[4] Ellis MJ, Tao Y, Lin L, Evans DB, Miller WR, Weber J (2006) High nuclear p27(kip1) levels predicts sensitivity to neoadjuvant letrozole in ER plus breast cancer independent of pAKT levels, PIK3CA mutation status and cell cycle effects: a potential role for p27(kip1) in predicting enhanced autophagocytosis in response to aromatase inhibitor therapy. Breast Cancer Res Treat 100:S187

[5] Yang Y, Zhang H, Lin Z-H, Zhou YS, Jing Q, Su Y (2013) Human skin based triboelectric nanogenerators for harvesting biomechanical energy and as self-powered active tactile sensor system. ACS Nano 7:9213–9222

[6] Hu Y, Yang J, Jing Q, Niu S, Wu W, Wang ZL (2013) Triboelectric nanogenerator built on suspended 3D spiral structure as vibration and positioning sensor and wave energy harvester. ACS Nano 7:10424–10432

[7] Lipomi DJ, Vosgueritchian M, Tee BC, Hellstrom SL, Lee JA, Fox CH (2011) Skin-like pressure and strain sensors based on transparent elastic films of carbon nanotubes. Nat Nanotechnol 6:788–792

[8] Fan F-R, Lin L, Zhu G, Wu W, Zhang R, Wang ZL (2012) Transparent triboelectric nanogenerators and self-powered pressure sensors based on micropatterned plastic films. Nano Lett 12:3109–3114

[9] Li C, Hesketh P, Maclay G (1994) Thin gold film strain gauges. J Vac Sci Technol, A 12:813–819
[10] Lacour SP, Chan D, Wagner S, Li T, Suo Z (2006) Mechanisms of reversible stretchability of thin metal films on elastomeric substrates. Appl Phys Lett 88:204103
[11] Li T, Huang Z, Xi Z, Lacour SP, Wagner S, Suo Z (2005) Delocalizing strain in a thin metal film on a polymer substrate. Mech Mater 37:261–273
[12] Rajanna K, Mohan S (1987) Longitudinal and transverse strain sensitivity of gold film. J Mater Sci Lett 6:1027–1029
[13] Neugebauer C, Webb M (1962) Electrical conduction mechanism in ultrathin, evaporated metal films. J Appl Phys 33:74–82
[14] Parker R, Krinsky A (1963) Electrical resistance strain characteristics of thin evaporated metal films. J Appl Phys 34:2700–2708
[15] Olichwer N, Leib EW, Halfar AH, Petrov A, Vossmeyer T (2012) Cross-linked gold nanoparticles on polyethylene: resistive responses to tensile strain and vapors. ACS Appl Mater Interface 4:6151–6161
[16] Moreira H, Grisolia J, Sangeetha NM, Decorde N, Farcau C, Viallet B (2013) Electron transport in gold colloidal nanoparticle-based strain gauges. Nanotechnology 24:095701
[17] Farcau C, Sangeetha NM, Moreira H, Viallet B, Grisolia J, Ciuculescu-Pradines D (2011) High-sensitivity strain gauge based on a single wire of gold nanoparticles fabricated by stop-and-go convective self-assembly. ACS Nano 5:7137–7143
[18] Brust M, Bethell D, Kiely CJ, Schiffrin DJ (1998) Self-assembled gold nanoparticle thin films with nonmetallic optical and electronic properties. Langmuir 14:5425–5429
[19] Herrmann J, Müller K-H, Reda T, Baxter G, Raguse Bd, De Groot G (2007) Nanoparticle films as sensitive strain gauges. Appl Phys Lett 91:183105
[20] Jiao W, Yi L, Zhang C, Wu K, Li J, Qian L (2014) Electrical conduction of nanoparticle monolayer for accurate tracking of mechanical stimulus in finger touch sensing. Nanoscale 6:13809–13816
[21] Huang M, Pascal TA, Kim H, Goddard WA III, Greer JR (2011) Electronic–mechanical coupling in graphene from in situ nanoindentation experiments and multiscale atomistic simulations. Nano Lett 11:1241–1246
[22] Jia J, Shi D, Feng X, Chen G (2014) Electromechanical properties of armchair graphene nanoribbons under local torsion. Carbon 76:54–63
[23] Hod O, Scuseria GE (2009) Electromechanical properties of suspended graphene nanoribbons. Nano Lett 9:2619–2622
[24] Hayashida T, Pan L, Nakayama Y (2002) Mechanical and electrical properties of carbon tubule nanocoils. Phys B Condens Matter 323:352–353
[25] Chen X, Zhang S, Dikin DA, Ding W, Ruoff RS, Pan L (2003) Mechanics of a carbon nanocoil. Nano Lett 3:1299–1304
[26] Deng C, Pan L, Ma H, Cui R (2015) Electromechanical vibration of carbon nanocoils. Carbon 81:758–766
[27] Ma H, Nakata K, Pan L, Hirahara K, Nakayama Y (2014) Relationship between the structure of carbon nanocoils and their electrical property. Carbon 73:71–77
[28] Sun Y, Wang C, Pan L, Fu X, Yin P, Zou H (2016) Electrical conductivity of single polycrystalline-amorphous carbon nanocoils. Carbon 98:285–290
[29] Ma H, Pan L, Zhao Q, Zhao Z, Qiu J (2012) Thermal conductivity of a single carbon nanocoil measured by field-emission induced thermal radiation. Carbon 50:778–783
[30] Li DW, Pan LJ, Qian JJ, Ma H (2009) High efficient synthesis of carbon nanocoils by catalysts produced by a Fe and Sn containing solution. Adv Mater Res 60:251–255
[31] Deng C, Pan L, Ma H, Hirahara K, Nakayama Y (2016) Flexible electrical probes made of carbon nanotube bundles. Carbon 101:331–337
[32] Dingle R (1950) The electrical conductivity of thin wires. Proc R Soc Lond A 201:545–560